Mutual Interaction between Surface Waves and Langmuir Circulations Observed in Wave-Resolving Numerical Simulations

YASUSHI FUJIWARA[a]

Graduate School of Science, Kyoto University, Kyoto, and Research Fellow of Japan Society for the Promotion of Science, University of Tokyo, Tokyo, Japan

YUTAKA YOSHIKAWA

Graduate School of Science, Kyoto University, Kyoto, Japan

(Manuscript received 22 November 2019, in final form 13 June 2020)

ABSTRACT

Wave-resolving simulations of monochromatic surface waves and Langmuir circulations (LCs) under an idealized condition are performed to investigate the dynamics of wave–current mutual interaction. When the Froude number (the ratio of the friction velocity of wind stress imposed at the surface and wave phase speed) is large, waves become refracted by the downwind jet associated with LCs and become amplitude modulated in the crosswind direction. In such cases, the simulations using the Craik–Leibovich (CL) equation with a prescribed horizontally uniform Stokes drift profile are found to underestimate the intensity of LCs. Vorticity budget analysis reveals that horizontal shear of Stokes drift induced by the wave modulation tilts the wind-driven vorticity to the downwind direction, intensifying the LCs that caused the waves to be modulated. Such an effect is not reproduced in the CL equation unless the Stokes drift of the waves modulated by LCs is prescribed. This intensification mechanism is similar to the CL1 mechanism in that the horizontal shear of the Stokes drift plays a key role, but it is more likely to occur because the shear in this interaction is automatically generated by the LCs whereas the shear in the CL1 mechanism is retained only when a particular phase relation between two crossing waves is kept locked for many periods.

1. Introduction

Langmuir circulations (LCs; Langmuir 1938) are roll circulations that arise in the surface mixed layer through the interaction of surface waves and currents. They regulate the air–sea fluxes of heat, momentum, and materials through turbulent mixing (D'Asaro 2014) and are considered to be a large uncertainty in the present climate modeling (Belcher et al. 2012). Dynamical understanding of LCs is necessary to construct better parameterizations and to obtain a better understanding of air–sea interaction.

To quantify the effects of LCs, simulations using the Craik–Leibovich (CL) equation (Craik and Leibovich 1976) are routinely performed. The CL equation is an equation of motion about the wave-averaged (nonoscillatory) flow field, where the residual wave effect is represented as the vortex force term and the Bernoulli head gradient term (Leibovich 1980; McWilliams et al. 2004). In the formation of LCs, the vortex force, which represents vorticity advection and tilting due to the wave-induced Stokes drift, plays a central role (e.g., Fujiwara et al. 2019). When there is a vertically sheared Stokes drift (i.e., deep- or intermediate-water waves) and vertically sheared current (typically produced by wind) in the same direction as the Stokes drift, vorticity tilting due to the Stokes drift causes instability to produce pairs of vortices aligned with the wind and wave direction. The resulting circulations are accompanied by downwind jet currents at the downwelling regions. This instability mechanism is called the CL2 mechanism (Craik 1977; Leibovich 1977, 1983; see also Fig. 11b), and it is considered to be a major driving mechanism of the LCs.

The CL equation requires the Stokes drift profile to be prescribed. Since the CL2 mechanism only requires vertical shear of the Stokes drift, horizontally uniform

[a] Current affiliation: Graduate School of Frontier Sciences, University of Tokyo, Kashiwa, Chiba, Japan.

Corresponding author: Yasushi Fujiwara, yfujiwara@edu.k.u-tokyo.ac.jp

DOI: 10.1175/JPO-D-19-0288.1

Stokes drift profile is often prescribed using the linear monochromatic solution or its spectral superposition (Kenyon 1969) in simulations using the CL equation (e.g., Skyllingstad and Denbo 1995; McWilliams et al. 1997; Li et al. 2005). This treatment implicitly assumes that the waves are unaffected by the current field.

In reality, the LCs would also affect the waves, and the current-affected waves would possibly affect the LCs. However, the dynamics of mutually interacting waves and LCs are largely unexplored. Several studies incorporate the current effect on waves into the wave-averaged equation using the wave action conservation law (McWilliams et al. 2004; Smith 2006; Uchiyama et al. 2010). However, the wave action law is only valid for the current structure that slowly changes in time and space relative to the wave period and wavelength. For LCs whose spatial scale is comparable to (or smaller than) the wavelength, such an approach cannot be used. Using an explicit simulation of wave motions and LCs, Kawamura (2000) reported that the wave amplitude varies in crosswind direction corresponding to the pattern of LCs, but he did not investigate the influence of the modulated wave field on the current field. Allowing the waves to be modulated in crosswind direction as observed in Kawamura (2000) and the laboratory experiment of Veron and Melville (2001) and Phillips (2005) conducted a linear stability analysis of sheared currents interacting with waves. There, the current velocity was assumed to be comparable to wave phase speed, which is relevant to LCs with laboratory scales [$\sim O(1)$ cm] rather than mixed layer scales in the ocean [$\sim O(10)$ m]. Recently, Suzuki (2019) investigated the dynamics of mutually interacting waves and a simplified LC-like current field under certain scaling conditions, where the wave action conservation was not assumed. He showed that the waves would change in time due to the current effect, and the CL equation will become invalid in such a case.

Thanks to advances in numerical models and computational resources, explicit numerical simulations of wave motions and underlying currents (called wave-resolving simulations or WRS) have become possible (Kawamura 2000; Guo and Shen 2013, 2014; Tsai et al. 2013, 2015, 2017; Wang and Özgökmen 2018; Fujiwara et al. 2018; Xuan et al. 2019). Since WRS does not rely on various assumptions behind the CL equation or the wave action law, it is a useful approach to explore processes that are not (or cannot be) incorporated in such theoretical frameworks. Also, WRS is suitable for identifying the dynamics of simulated phenomena because one can evaluate a closed budget of various quantities with highly controllable experiments.

In this study, we conduct a series of idealized WRS to investigate currents' effect on waves and its possible impact on LCs. Simulations with the CL equation are also conducted for comparative study. Small-scale turbulence effect is represented with constant viscosity (not like LES) to avoid complications of dynamics due to turbulence parameterizations. Focusing on vorticity, the differences between the WRS with explicit wave motions and the CL equation with prescribed Stokes drift are analyzed using a new approach of budget analysis in a deformable domain.

The organization of this paper is as follows. In section 2, the experimental settings and the numerical model are described. In section 3, the analysis framework is introduced. In section 4, the simulation results are described, and the vorticity budget is analyzed to explain the result. In section 5, the results are summarized, and the implications of the results obtained here are discussed.

2. Experimental design

Consider an incompressible homogeneous fluid with uniform and isotropic viscosity. Let us denote the Cartesian coordinates with x, y, z and time with t. Here, z is taken vertically upward. Throughout this paper, vectors represent the two horizontal components like $\mathbf{x} = (x, y)$. Consider a horizontally rectangular domain bounded by a flat rigid bottom at $z = -H$ and a freely deformable upper surface at $z = \eta(\mathbf{x}, t)$, which is assumed to be single-valued (no overturn of the surface). The fluid motion follows the incompressible Navier–Stokes equation in a nondimensional form:

$$\partial_t u + \mathbf{u}\cdot\nabla u + w\partial_z u = -\partial_x(\eta + p) + \nabla\cdot\mathbf{T}^{\mathbf{x}x} + \partial_z \mathbf{T}^{zx}, \tag{1}$$

$$\partial_t v + \mathbf{u}\cdot\nabla v + w\partial_z v = -\partial_y(\eta + p) + \nabla\cdot\mathbf{T}^{\mathbf{x}y} + \partial_z \mathbf{T}^{zy}, \tag{2}$$

$$\partial_t w + \mathbf{u}\cdot\nabla w + w\partial_z w = -\partial_z p + \nabla\cdot\mathbf{T}^{\mathbf{x}z} + \partial_z \mathbf{T}^{zz}, \quad \text{and} \tag{3}$$

$$\nabla\cdot\mathbf{u} + \partial_z w = 0. \tag{4}$$

Here, u, v, w are the velocity components in x, y, and z directions, respectively. Horizontal velocity is denoted as $\mathbf{u} \equiv (u, v)$. The symbol $\nabla \equiv (\partial_x, \partial_y)$ is horizontal derivative operator following constant z, p is the nonhydrostatic part of kinematic pressure, and $\mathbf{T}^{ij}$ are the viscous stress tensor components. All the variables are nondimensionalized in terms of the wavenumber k_d and the phase speed c_d of a reference linear deep-water wave [whose dispersion relation is $c_d = (g_d/k_d)^{1/2}$ using the dimensional gravitational acceleration g_d], with subscript d meaning dimensional. The nondimensional phase speed c for the linear deep-water wave and wavenumber k are both unity, but we explicitly use c and k in the following equations and expressions for easy understanding of them. The stress tensor is defined as follows:

$$\mathbf{T}^{\mathbf{xx}} = \nu[\nabla\mathbf{u} + (\nabla\mathbf{u})^{\mathrm{T}}],$$

$$\mathbf{T}^{\mathbf{x}z} = \mathbf{T}^{z\mathbf{x}\mathrm{T}} = \nu(\nabla w + \partial_z \mathbf{u}), \quad \text{and}$$

$$\mathbf{T}^{zz} = 2\nu\partial_z w$$

Here, $\nu \equiv \nu_d/(c_d k_d^{-1})$ is the nondimensional kinematic viscosity based on the linear wave quantities and the dimensional kinematic viscosity ν_d. The surface elevation η follows the volume conservation equation:

$$\partial_t \eta = -\nabla \cdot \int_{-H}^{\eta} \mathbf{u}\, dz. \tag{5}$$

The reference level $z = 0$ is chosen so that $\eta = 0$ when the fluid is at rest.

The horizontal boundaries are prescribed to be doubly periodic. At the upper surface, the horizontal momentum flux of $\tau^{\mathbf{x}}$ per unit horizontal area is imposed through tangential viscous stress. The bottom boundary condition is free-slip.

We are interested in the interaction of developed LCs and freely propagating waves. To shorten the simulation period, the flow field is initialized with the LC field produced using the CL equation:

$$\partial_t u + \mathbf{u}\cdot\nabla u + w\partial_z u = -\partial_x \Pi + \nabla\cdot\mathbf{T}^{\mathbf{x}x} + \partial_z \mathbf{T}^{zx}, \tag{6}$$

$$\partial_t v + \mathbf{u}\cdot\nabla v + w\partial_z v = -\partial_y \Pi + \nabla\cdot\mathbf{T}^{\mathbf{x}y} + \partial_z \mathbf{T}^{zy} - u^{\mathrm{St}}\zeta^z, \tag{7}$$

$$\partial_t w + \mathbf{u}\cdot\nabla w + w\partial_z w = -\partial_z \Pi + \nabla\cdot\mathbf{T}^{\mathbf{x}z} + \partial_z \mathrm{T}^{zz} + u^{\mathrm{St}}\zeta^y, \quad \text{and} \tag{8}$$

$$\nabla\cdot\mathbf{u} + \partial_z w = 0. \tag{9}$$

Here, the last terms in the rhs of Eqs. (7) and (8) are the vortex force terms, and the Stokes drift profile is prescribed as

$$u^{\mathrm{St}}(z) = (ak)^2 c(\tanh kH)^{1/2} \frac{\cosh 2k(z+H)}{2\sinh^2 kH}, \tag{10}$$

where a is the amplitude of the wave to be imposed. Here, $\zeta^x = \partial_y w - \partial_z v, \zeta^y = \partial_z u - \partial_x w$, $\zeta^z = \partial_x v - \partial_y u$ are the components of vorticity, and Π is the sum of the kinematic pressure and the Bernoulli head. Note that $c(\tanh kH)^{1/2}$ represents the nondimensional phase speed of the linear surface waves with finite depth. With our domain size (listed later), $\tanh kH$ is greater than 0.99, which corresponds to the deep-water regime. At the upper surface, constant tangential stress $\tau^{\mathbf{x}} = (\tau_0^x, 0)$ is imposed to represent the momentum input from the wind (τ_0^x is a constant). During the spinup simulations, the x direction body force $-\tau_0^x/H$ is imposed throughout the fluid to prevent the fluid from accelerating in the x direction. The CL equation is computed under rigid-lid condition (i.e., instead of deformable upper surface, we assume $\eta = 0$ and $w = 0$ at $z = 0$). Starting from weak noise, the spinup is run for more than 27 000 periods of the reference wave.

Two types of simulations are performed to study the differences arising from different representations of wave effects. In the wave-resolving simulations (labeled WRS), the wave motions are explicitly simulated. In the Craik–Leibovich simulations (labeled CL), the residual wave effects are parameterized as the vortex force using prescribed Stokes drift profiles. The upper surface of the fluid is treated as a free surface in WRS runs, and the rigid-lid condition is applied in CL runs. In WRS, it is difficult to obtain statistical quantities of LCs resulting from mutually interacting waves and currents because waves attenuate due to viscosity over time scales of LCs. Therefore, instead of making statistical comparisons between WRS and CL, we chose to make deterministic comparisons. Both runs are started from the spun-up LC field and integrated from $t = 0$ to $t = 120T$, where $T = 2\pi$ is a wave period of the reference wave. The simulation period of $120T$ is chosen because it is long enough for waves to respond to current structures (section 4a). It is confirmed that the instantaneous switching from rigid-lid to free surface upper boundary condition in WRS runs causes only small initialization shock [waves with amplitude $O(10^{-4}k^{-1})$].

At the beginning of the WRS run, impulsive pressure is imposed at the upper surface of the spun-up field to initiate a monochromatic propagating wave motion of amplitude a and wavenumber $k = 1$, using the delta-function method proposed by Guo and Shen (2009). After that, the pressure is set to zero at the surface, and the wave is freely propagated.

The viscous wave attenuation in the WRS run transfers the waves' momentum to underlying current. The current field feels this momentum transfer as additional tangential stress (called the virtual wave stress or VWS; Longuet-Higgins 1953) at the surface, which results in an intensification of LCs (Fujiwara et al. 2019, manuscript submitted to *Ocean Modell.*). However, this effect is not included in the CL equation. To make a meaningful comparison between WRS and CL runs, we must modify the stress boundary condition at the upper boundary to compensate for the VWS. In WRS runs, the x-component stress $\tau_0^x - \tau_{\mathrm{VWS0}}^x$ is imposed at the surface, where $\tau_{\mathrm{VWS0}}^x \equiv 2\nu a^2 k^3 c/(\tanh kH)^{1/2}$ is the VWS of the initially imposed wave. The term τ_{VWS0}^x is meant to offset the VWS effect. Using WRS, we have confirmed that the momentum flux via the wave attenuation can be successfully offset by reducing the surface stress (Fujiwara et al. 2019, manuscript submitted to *Ocean Modell.*).

The CL run is started from the same spun-up field, and the vortex force is imposed. Taking the viscous wave attenuation in the WRS into account, the Stokes drift profile in the CL run is prescribed as follows:

$$u^{\mathrm{St}}(z,t) = (ak)^2 c e^{-4\nu k^2 t} \frac{\cosh 2k(z+H)}{2k \sinh^2 kH}. \qquad (11)$$

The temporal decay rate $\exp(-4\nu k^2 t)$ is calculated from the linear solution of decaying viscous wave (Lamb 1932).

In the CL run, the x-component stress $\tau_0^x - \tau_{\mathrm{VWS0}}^x + \tau_{\mathrm{VWS0}}^x e^{-4\nu k^2 t}$ is imposed at the surface. The first two terms are the stress imposed in the WRS run, and the third term is meant to address the weakening of the actual VWS in the WRS run due to wave attenuation. These treatments assume that the waves in WRS runs attenuate following the linear solution of viscous wave and that the VWS is horizontally uniform, so the offset of the VWS effect is only approximately achieved.

The simulations are conducted with various combinations of experiment parameters (explained below) and domain size. They are listed in Table 1. The experiments are characterized with three nondimensional parameters: the Froude number (relative strength of wind-driven shear flow to reference wave phase speed) $\mathrm{Fr} = u_*/c$, the wave slope ak, and the Reynolds number $\mathrm{Re} = ck^{-1}/\nu$, where $u_* \equiv (\tau_0^x)^{1/2}$ is the friction velocity associated with the wind-driven shear flow. Combining Fr and ak, the turbulent Langmuir number (McWilliams et al. 1997) can be represented as $\mathrm{La} = (u_*/u^{\mathrm{St}}|_{z=0})^{1/2} = \mathrm{Fr}^{1/2}(ak)^{-1}$, where we assumed a deep-water wave and evaluated $u^{\mathrm{St}}|_{z=0}$ as $(ak)^2 c$. Using the wind stress bulk formula and the equilibrium significant waves (e.g., Holthuijsen 2010), we can make a rough estimate of $ak \approx 0.1$ and $\mathrm{Fr} \approx 0.001$ for the significant wave of fully developed seas. Therefore, the F10 case (Table 1) roughly corresponds to a condition with fully developed waves.

For Reynolds number, we can estimate the typical oceanic value as $\mathrm{Re} = O(10^6)$ using the molecular viscosity of water $O(10^{-6})\,\mathrm{m^2\,s^{-1}}$ and the reference wavelength of $O(10)$ m. Because of computational limitations, we must employ smaller Re than above, and we found that, for the F10 case, $\mathrm{Re} = 4 \times 10^4$ was adequate to suppress the development of eddies smaller than our grid spacings explained later. With larger values of ak and Fr and same grid spacings, smaller Re (stronger viscosity) is required to prevent the dissipation scale becoming smaller than the grid scale. To achieve this, we changed the viscosity so that the grid Reynolds number $U\Delta y/\nu$ (Δy is grid spacing in the crosswind direction) would become constant among cases,

TABLE 1. List of numerical experiments. Each case has WRS and CL runs. In experiment names, L, S, and N indicate domain size and signify long, shallow, and narrow, respectively.

Expt name	Fr	ak	Re	L_x/λ	L_y/λ	H/λ	La
F30	0.003	0.1	1.92×10^4	1	8	1	0.55
F20	0.002	0.1	2.52×10^4	1	8	1	0.45
F10	0.001	0.1	4.00×10^4	1	8	1	0.32
F30a07	0.003	0.071	2.42×10^4	1	8	1	0.77
F30a14	0.003	0.141	1.53×10^4	1	8	1	0.39
F30-S	0.003	0.1	1.92×10^4	1	8	0.5	0.55
F10-S	0.001	0.1	4.00×10^4	1	8	0.5	0.32
F30-NS	0.003	0.1	1.92×10^4	1	4	0.5	0.55
F20-NS	0.002	0.1	2.52×10^4	1	4	0.5	0.45
F10-NS	0.001	0.1	4.00×10^4	1	4	0.5	0.32
F10a07-NS	0.001	0.071	5.04×10^4	1	4	0.5	0.45
F10a14-NS	0.001	0.141	3.17×10^4	1	4	0.5	0.22
F30-LNS	0.003	0.1	2.52×10^4	2	4	0.5	0.55
F10-LNS	0.001	0.1	4.00×10^4	2	4	0.5	0.32

where the velocity scale $U = (u_*^2 u^{\mathrm{St}})^{1/3} = \mathrm{Fr}^{2/3}(ak)^{2/3}c$ is used (e.g., Li and Garrett 1993). This treatment successfully kept the smallest eddy scale roughly constant. Note that the Reynolds number used in our simulations is smaller by two orders of magnitude than the realistic value, so the viscous wave attenuation is enhanced. For example, in the F30 case, about 15% of wave energy is dissipated due to viscosity during the $120T$ simulation period. This attenuation and the associated VWS would become smaller with increased Reynolds number as in typical ocean conditions.

Several combinations of domain length L_x, width L_y, and depth H are used to investigate the influence of domain size on the simulation results. We take the cases with $(L_x, L_y, H) = (\lambda, 8\lambda, \lambda)$ as the "standard" case, and examine the domain size dependences by comparing it with "shallow" (labeled S, halved H), "narrow" (labeled N, halved L_y), and "long" (labeled L, doubled L_x) cases (Table 1). The domain is discretized with 128 grid points per wavelength in the x direction and with 256 grid points per wavelength in the y direction. In vertical, 96 and 160 grid points are taken for cases with $H = 0.5\lambda$ and λ, respectively. The vertical coordinate is transformed to a surface-following sigma coordinate (the coordinate spacing is uniformly stretched according to the surface elevation). The grid points are clustered near the surface, and the layer thickness at the top layer is set to 0.5δ, where $\delta \equiv (2\nu/ck)^{1/2}$ is the thickness of the oscillatory viscous boundary layer (Phillips 1966).

Because of the limited computational resource, we could not conduct simulations with a domain large enough to avoid its influence on wave modulation patterns. Especially, limited domain length $L_x = \lambda$ used in most cases tends to magnify the current effect on waves because the waves tend to propagate over the same current structure for many wave periods. However, the current structure of LCs is typically elongated in the wave propagation direction, so we should still be able to obtain meaningful understandings of the wave–current interaction processes.

Numerical model

The numerical model used here (Fujiwara et al. 2019, manuscript submitted to *Ocean Modell.*) solves the incompressible Navier–Stokes equation in a domain with a free surface at the top, with pseudospectral and finite-difference discretizations in the horizontal and vertical directions, respectively. As noted above, the vertical coordinate is transformed to the sigma coordinate. Since no approximations are made regarding the surface slope, the model can correctly simulate the large-amplitude waves, as long as there is no overturn of the upper surface (breaking). The model is designed with special attention to momentum and energy conservation properties so that the simulated wave–current interaction would not be contaminated by numerical errors. Especially, the model is capable of accurately simulating the momentum transfer from decaying viscous waves to currents. For a more detailed description of the model and the test results, see Fujiwara et al. (2019, manuscript submitted to *Ocean Modell.*).

3. Analysis method

To investigate the dynamical coupling between waves and currents, we need to separate these two types of motion. Guo and Shen (2013, 2014) used an Eulerian temporal average on a reference frame moving with the wave phase speed, where the average and the deviation represent wave motions and turbulence, respectively. This approach cannot be used when the wave pattern changes in time due to wave dispersion or modulation. Fujiwara et al. (2018) used an Eulerian temporal average on a fixed frame, where the average and the deviation represent currents and wave motions, respectively. This approach cannot handle the regions above wave trough because the Eulerian average cannot be defined there.

To avoid such problems, we use a vertically stretched coordinate system for analysis. This approximates the mathematical framework introduced by Mellor (2003) and Aiki and Greatbatch (2012) into the context of ocean surface waves, called the vertically semi-Lagrangian horizontally Eulerian (VL) coordinate system. In this framework, a location in fluid and time are specified with $(\tilde{\mathbf{x}}, \tilde{z}, \tilde{t})$, which is related to the Cartesian coordinates and time $(\mathbf{x}, z, t)$ with

$$\mathbf{x} = \tilde{\mathbf{x}}, z = z(\tilde{\mathbf{x}}, \tilde{z}, \tilde{t}), t = \tilde{t}. \tag{12}$$

The vertical coordinate $\tilde{z}$ is defined so that the surfaces of constant $\tilde{z}$ (hereinafter $\tilde{z}$ surfaces) would follow the wave motion. For instance, when there is a small-amplitude irrotational wave with amplitude a and wavenumber k, and $\eta = a\cos k\tilde{x}$, the $\tilde{z}$ surfaces are

$$z(\tilde{x}, \tilde{z}) = \tilde{z} + a\frac{\sinh k(\tilde{z} + H)}{\sinh kH}\cos k\tilde{x} \tag{13}$$

to the leading order.

The analysis on the VL coordinate is conducted by first diagnosing the location of $\tilde{z}$ surfaces for each value of $\tilde{z}$ from the instantaneous η, and then interpolating the variables in the model (defined at grid points of sigma-coordinate) onto the depth of $\tilde{z}$ surfaces. Using horizontal Fourier transform, the instantaneous η is decomposed into Fourier series of horizontal wavenumber:

$$\eta(\tilde{\mathbf{x}}) = \sum_{\mathbf{k}} f_\eta(\mathbf{k}) \cos[\tilde{\mathbf{x}} \cdot \mathbf{k} - \alpha_\eta(\mathbf{k})],$$

where $\mathbf{k}$ is horizontal wavenumber vector, f_η is the real-valued Fourier coefficient, and α_η is real-valued phase shift. Approximating the displacement of $\tilde{z}$ surfaces with the linear solution, they are diagnosed as follows:

$$z(\tilde{\mathbf{x}}, \tilde{z}) = \tilde{z} + \sum_{\mathbf{k}} f_\eta(\mathbf{k}) \frac{\sinh|\mathbf{k}|(\tilde{z} + H)}{\sinh|\mathbf{k}|H} \cos[\tilde{\mathbf{x}} \cdot \mathbf{k} - \alpha_\eta(\mathbf{k})]. \tag{14}$$

The upper surface $z = \eta$ is represented as the $\tilde{z}$ surface $\tilde{z} = 0$. Therefore, this coordinate transformation maps the domain $-H \le z \le \eta$ to $-H \le \tilde{z} \le 0$.

In this framework, a scalar conservation equation $\partial_t \varphi + \mathbf{u} \cdot \nabla \varphi + w \partial_z \varphi = S^\varphi$ (φ is a scalar concentration, and S^φ is a source term) is transformed to the following form:

$$\partial_{\tilde{t}}(h\varphi) + \tilde{\nabla} \cdot (h\mathbf{u}\varphi) + \partial_{\tilde{z}}(h\omega\varphi) = hS^\varphi, \tag{15}$$

where $\tilde{\nabla} \equiv (\partial_{\tilde{x}}, \partial_{\tilde{y}})$ is horizontal derivative operator following $\tilde{z}$ surfaces, $h \equiv \partial_{\tilde{z}} z$ is the normalized layer thickness, and $\omega \equiv h^{-1}[w - (\partial_{\tilde{t}} + \mathbf{u} \cdot \tilde{\nabla})z]$ is the velocity across the $\tilde{z}$ surfaces. Since the $\tilde{z}$ surfaces approximately follow the wave motions, ω should only contain the nonoscillatory vertical motions. Denoting the wave-average with an overline, this requirement is written as $\omega = \overline{\omega}$, where the wave-average is defined as the temporal average over several wave periods following constant $(\tilde{\mathbf{x}}, \tilde{z})$. The requirement is only approximately achieved because it is assumed that the waves follow the irrotational linear solution in the evaluation of $\tilde{z}$ surfaces. The performance of the analysis (how well the $\tilde{z}$ surfaces follow the wave motion) is examined in the appendix using the WRS result. It should be noted that Eq. (15) is exact regardless of the evaluation method, so exact budget analysis is possible even if $\omega = \overline{\varpi}$ is not strictly achieved.

The thickness-weighted mean of φ is defined as $\hat{\varphi} \equiv \overline{h\varphi}/\overline{h}$. The thickness-weighted mean velocity $\hat{\mathbf{u}}$ is the mass transport velocity, which corresponds to the Lagrangian mean velocity.

This analysis framework has the following merits. First, the whole water column, including the levels above the wave crest, can be analyzed. This allows us closed budget analyses of conserved quantities. Second, the surface wave field does not need to be monochromatic or nondispersive. Third, the (thickness-weighted) averaged quantities have clear physical meanings (e.g., mass transport velocity). This is an advantage over the sigma coordinate, where the averages depend on domain depth even when the phenomenon is independent of domain depth, like deep-water waves. Finally, only one-dimensional interpolation is needed to evaluate the variables on the VL coordinate grid points from the model results defined at the sigma-coordinate grid points. Thanks to this feature, the computational cost is reduced compared to the classical Lagrangian or the generalized Lagrangian mean (Andrews and McIntyre 1978) frameworks. Also, the conservation equation [Eq. (15)] is significantly simpler compared with such three-dimensional Lagrangian frameworks.

We developed a code to perform an online analysis based on the VL framework. At the time steps when the variables are evaluated, the location of the $\tilde{z}$ surfaces is first calculated from the instantaneous $\eta(\mathbf{x}, t)$, and then variables are interpolated to the $\tilde{z}$ surfaces. To reduce the computational cost while retaining the accuracy of phase average, evaluations are typically conducted every 1/100 of the reference wave period (once in 2–4 integration steps).

To separate the effect of the Stokes drift, the mass transport velocity $\hat{\mathbf{u}}$, $\hat{w}$ are decomposed into Stokes and current components. Helmholtz decomposition is applied to the instantaneous velocity field $\mathbf{u}$, w:

$$\mathbf{u} = \mathbf{u}^p + \mathbf{u}^r, \; w = w^p + w^r,$$

where superscripts p and r denote potential and rotational components, respectively. Then the thickness-weighted average is applied to each component. Assuming that the wave motion is nearly irrotational, the Stokes drift velocity is evaluated as $\mathbf{u}^{\mathrm{St}} \equiv \hat{\mathbf{u}}^p$ and $w^{\mathrm{St}} \equiv \hat{w}^p$. The current velocity is evaluated as $\mathbf{u}^{\mathrm{cur}} \equiv \hat{\mathbf{u}}^r$ and $w^{\mathrm{cur}} \equiv \hat{w}^r$. After horizontal averaging, the evaluated Stokes drift profile agrees well with the classical solution, as shown in the appendix.

In the CL simulations, h and $z(\tilde{\mathbf{u}}, \tilde{z}, \tilde{t})$ are identically 1 and $\tilde{z}$, respectively. In the analyses, the prognostic variable of the CL equation is treated as the current velocity ($\mathbf{u}^{\mathrm{cur}}$, w^{cur}), and the prescribed Stokes drift profile in the vortex force term Eq. (11) is used as ($\mathbf{u}^{\mathrm{St}}$, w^{St}).

4. Results

In this section, we mainly present the result of the F30 case (Table 1), where the newly found wave–current interaction process was most prominent. The parameters of the F30 case, Fr = 0.003 and ak = 0.1, correspond to a relatively young sea.

a. Velocity field and wave modulation of WRS

First, the velocity field of the WRS run of the F30 case is presented. Hereinafter, unless noted, wave-averaged quantities such as u^{cur} and u^{St} are obtained by temporally averaging over $115T \le t \le 120T$. Figure 1 shows the horizontal (at $\tilde{z} = -0.05\lambda$) and vertical (at $x = 0$) sections of u^{cur} and w^{cur} in WRS of F30. Downwind jet pattern near the surface and collocated downwelling motions can be observed. The crosswind velocity v^{cur} (not shown) is convergent above the downwelling regions and divergent below, showing the roll structure. These are typical features of LCs. It can be also seen that the circulations are multiscale. The region $2.5\lambda \lesssim y \lesssim 4\lambda$ is the large-scale downwelling zone, and the downwind jet is strongest over this region. This region also corresponds to the large-scale downwind jet. This large-scale LC spans over the whole domain width, and its horizontal extent seems to be limited by the domain size.

Next, the impact of the current field on the waves is presented. Shown in Fig. 2 are the snapshots of the surface displacement η at t = 20, 70 and 120T, the x-component surface Stokes drift $u^{\mathrm{St}}(\tilde{z} = 0)$, and x-averaged downwind current velocity $u^{\mathrm{cur}}(\tilde{z} = -0.5)$ obtained from the WRS of F30. Stewart and Joy (1974) showed that, for a simplified current structure, the deep-water waves are affected by the current velocity roughly at the depth of $\tilde{z} = -0.5 = \lambda/4\pi$. The wave amplitude becomes modulated in the y direction. Consistently with the amplitude modulation, the x-component Stokes drift changes in y. It was found that the y- and z-component Stokes drift was smaller than the x component by one or more orders of magnitude.

The spatial pattern of the wave amplitude and the x-component current velocity field u^{cur} show that the wave energy is concentrated over a band where u^{cur} is small (Figs. 1 and 2). A similar wave modulation is reported in Kawamura (2000). Note that only large-scale current structures (larger than about λ in y) seem to affect the wave modulation patterns. From these, we can speculate

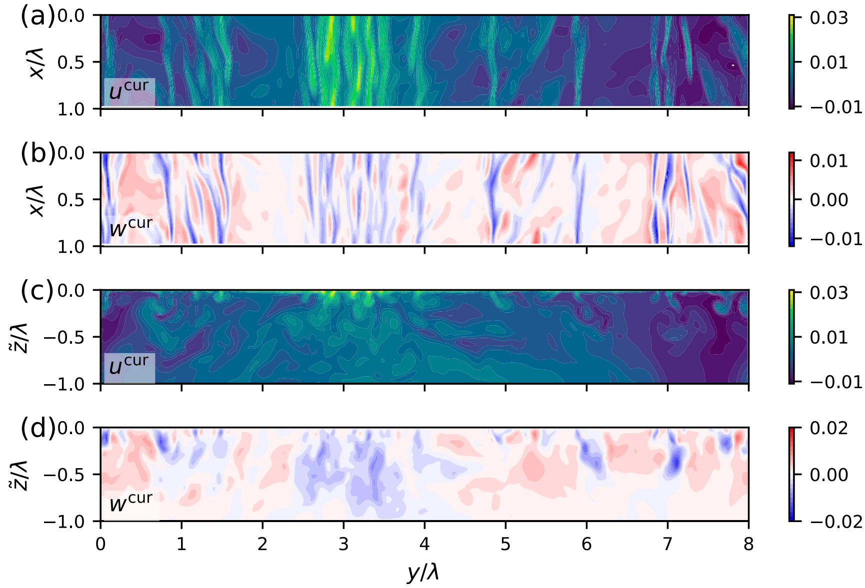

FIG. 1. Top views of (a) downwind current velocity u^{cur} and (b) vertical current velocity w^{cur} at $\tilde{z} = -0.05\lambda$, and y–$\tilde{z}$ cross sections (at $x = 0$) of (c) u^{cur} and (d) w^{cur} from WRS of F30. Variables are temporally averaged over $115T \le t \le 120T$.

that the jet-like current structure associated with the LCs refracted the waves because the waves are likely to be affected by the current structure larger than the wavelength. As shown in Fig. 2, the intensity of modulation changes in time. This temporal variation of the modulation will be discussed in the next section.

b. Parameter dependence of wave modulation

Next, we shall further investigate the intensity of wave modulation by comparing the WRS of different experimental parameters. We first compare the result of F30 and F30-S (the same as F30 except for the half domain depth) to study how differences in the current field affect the wave modulation and then try to infer the general parameter dependence of wave modulation.

Figure 3 shows the horizontal and vertical sections of u^{cur} and w^{cur} of F30-S. As in F30 (Fig. 1), we can clearly see the features of LCs. The multiscale circulation structure is less evident in F30-S, but we can still see the large-scale downwind jet in the regions $3.5\lambda \lesssim y \lesssim 5\lambda$ and $6\lambda \lesssim y \lesssim 8\lambda$. Unlike in the F30 case, the horizontal extent of the large-scale LCs is smaller than the domain width. Also, the downwind velocity of the large-scale LCs is small relative to F30 (see also Fig. 2). We consider that the shallow geometry of the F30-S case prohibited the formation of horizontally large-scale cells to keep the aspect ratio of cell structure close to unity.

Compared to F30, the wave modulation (Fig. 2) is weaker in F30-S, while the spatial pattern of the modulation (the amplitude is small over the jet) is consistent with F30. The fact that the modulation is weaker in F30-S is consistent with the idea of wave refraction. Since the largest scale of the jet is smaller relative to F30, the currents are less likely to refract the waves.

Next, we compare the wave modulation intensity of cases with different parameters and domain sizes. At each time and location y, wave amplitude $A(y)$ was calculated by taking the Fourier transform of η in x, and taking its first coefficient. Then wave modulation is measured with $a^{-1}[\max A(y) - \min A(y)]$. Figure 4 shows the temporal change of the amplitude modulation for cases with different forcing parameters and domain size. It can be seen that the wave modulation is stronger in cases with larger Fr and smaller *ak*. As explained below, these parameters seem to determine the features (crosswind variation of u^{cur}) of the LCs, and the features determine the strength of modulation. Also, the comparison between cases with different domain sizes (right panel of Fig. 4) shows that the wave modulation is stronger for cases with increased domain size in crosswind (y) and vertical (z) directions and smaller domain length in downwind (x) direction.

The dependences on Fr and *ak* can be understood through the downwind current u^{cur} of the initial Langmuir circulation field, which causes the waves to be refracted and modulated. As shown in Fig. 5a, comparing the cases with the same domain sizes, the amplitude modulation is strongly correlated with the horizontal standard deviation of initial u^{cur}. Here, the horizontal standard deviation is mostly attributed to the crosswind variation of u^{cur} (see, e.g., Fig. 1). From the studies using the CL

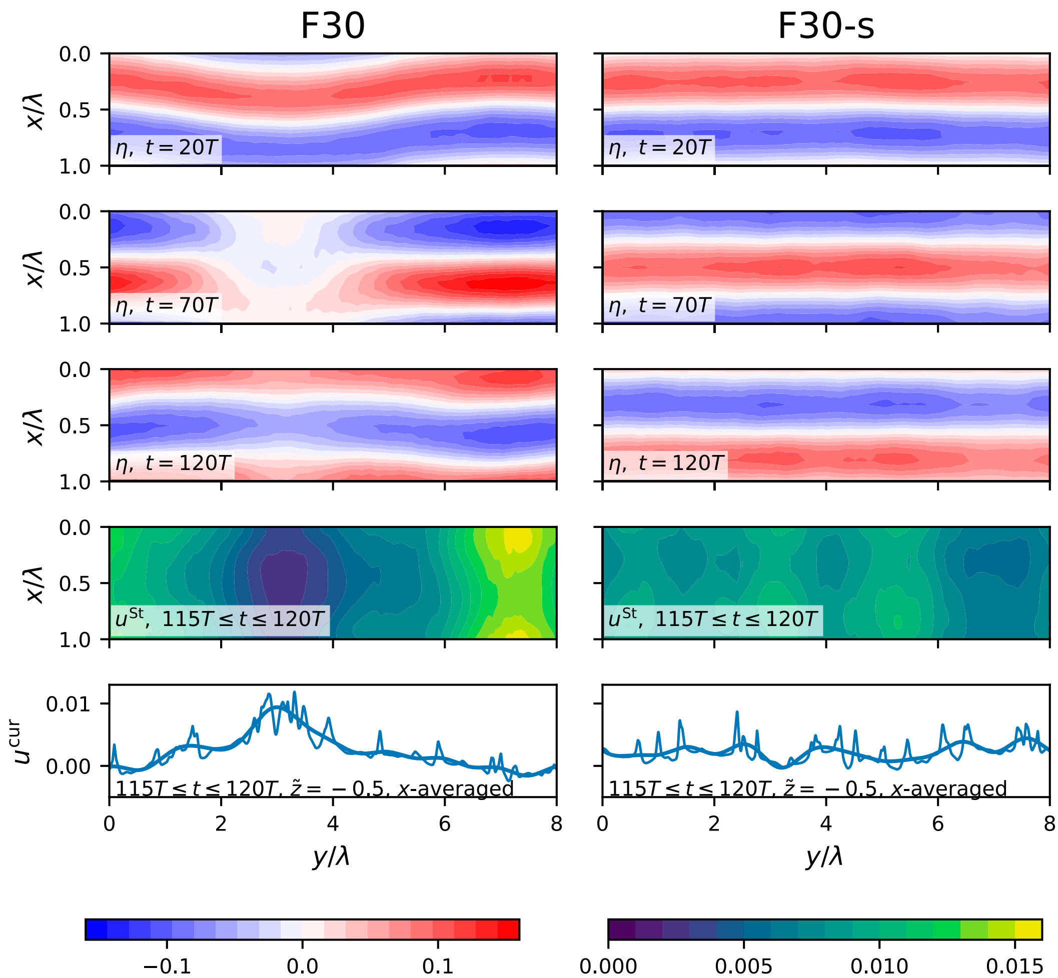

FIG. 2. Top views of surface elevation η at $t = 20$, 70, and $120T$, x-component Stokes drift u^{St} at the water surface, and x-averaged downwind current u^{cur} at $\tilde{z} = -0.5$. Wave-averaged velocities u^{St} and u^{cur} are temporally averaged over $115T \leq t \leq 120T$. In the panels of u^{cur}, the horizontally low-pass-filtered (with the cutoff wavelength of λ) profile is shown with thick solid lines. Shown are the results from WRS of (left) F30 and (right) F30-S. The lower-left and lower-right color bars are for η and u^{St}, respectively.

equation, it is known that the variance of u^{cur} increases with $\mathrm{La} = \mathrm{Fr}^{1/2}(ak)^{-1}$ (Li et al. 2005). Consistently with this, we find that the amplitude modulation is greater with larger La (Fig. 5b). Therefore, the horizontal variation of u^{cur} is greater for larger Fr and smaller ak. Also, as discussed above, a wider and deeper domain leads to stronger modulation because the domain size in the y and z directions regulates the maximum size of Langmuir cells. On the other hand, with a domain longer in the x direction, wave modulation becomes weaker. We speculate that this is because the Langmuir cells become less uniform in the x direction, and the currents' effect becomes less concentrated on particular regions.

Note that the waves are modulated even in the F10 case ($\mathrm{Fr} = 0.001$; $ak = 0.1$), which corresponds to typical parameter values in the fully developed sea. The surface Stokes drift at the strongest location is about 50% stronger compared to the weakest location. This implies that the LCs under typical values of ak and Fr may affect the spatial pattern of major waves (like significant waves). Because the various limitations of our simulation may be quantitatively affecting the result, the examination with the actual water is desirable. The current effect on waves will be observed through the crosswind variation of wave amplitude associated with the spatial pattern of the LCs. Because it is difficult to precisely measure the spatial distribution of wave amplitude in the field, laboratory experiments would be a good start point to examine the effect. The effects of idealization in our simulations are further discussed in section 5.

In cases such as F30 and F30a07 ($\mathrm{Fr} = 0.003$; $ak = 0.07$), the modulation first grows in time, takes its peak

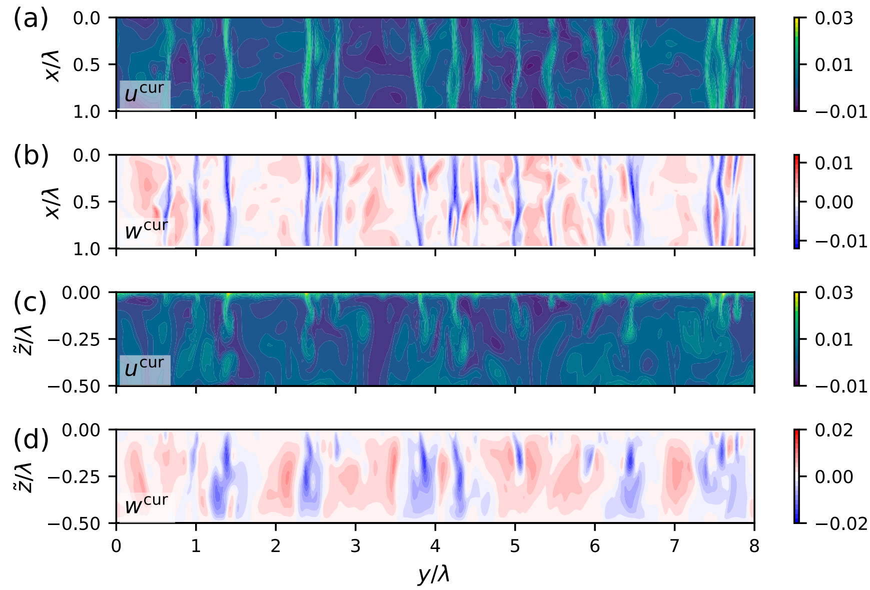

FIG. 3. As in Fig. 1, for WRS of the case F30-S.

(at around $t = 70T$ in F30), and then decays (Fig. 4). Some additional experiments showed that the modulation repeats the growth and decay while retaining the spatial pattern of smaller amplitude over and larger amplitude off the downwind jet. In the growing stage of the modulation, the initially linear isophase lines were bent forward above the jet current (Fig. 2, $t = 20T$ of F30). At the maximum of modulation, the isophase lines above the jet become disconnected from the ambient region and then reconnected with the lines of one period ahead. After the reconnection, the isophase lines above the jet is advected forward and catch up with the ambient part as the modulation decays. This disconnection and reconnection of the isophase lines can be understood as advection and distortion of the isophase lines due to the y-varying downwind current. While this growth–decay process of wave modulation needs further investigation, in this paper we shall focus on the impact of modulated waves on the LCs.

c. *Comparison with the CL run*

Next, we compare WRS and CL results. Since the current effect on waves arises in large horizontal scales, we can expect its effect on LCs to arise at similar scales.

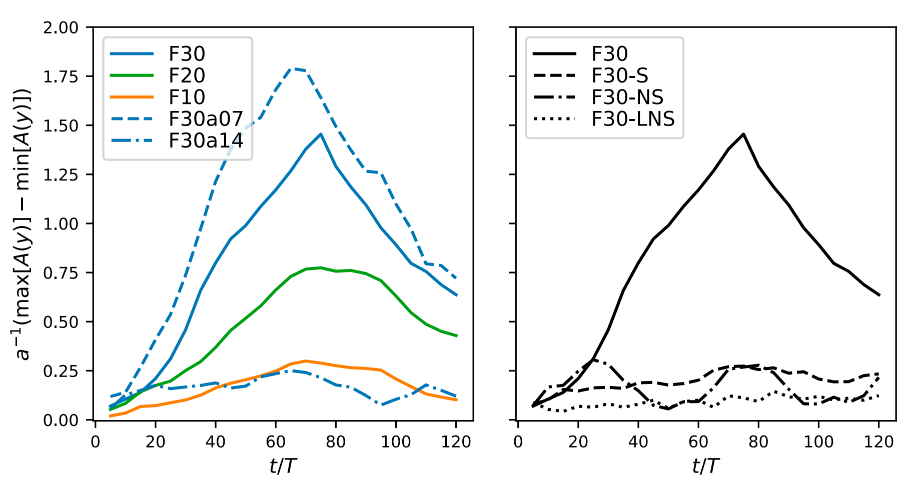

FIG. 4. Temporal evolution of normalized amplitude modulation $a^{-1}[\max A(y) - \min A(y)]$ of WRS runs: (left) comparison of cases with the "standard" domain size with different Fr and ak and (right) comparison of cases with different domain sizes.

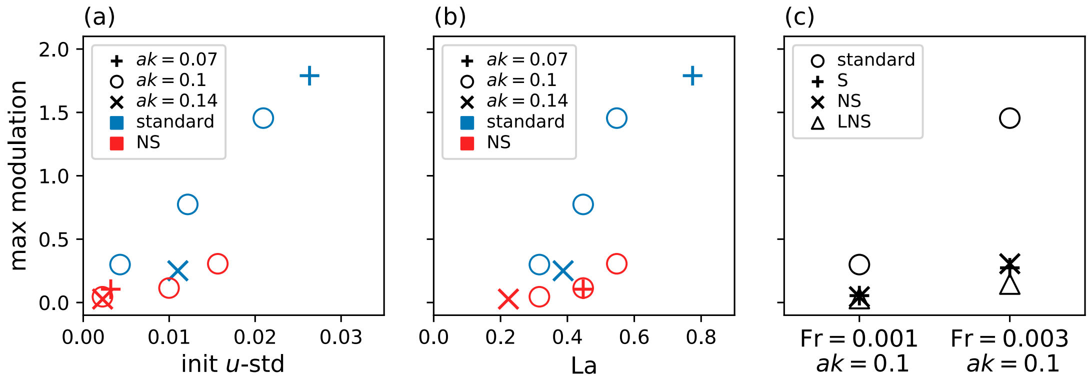

FIG. 5. Scatterplot of temporal maximum of normalized amplitude modulation $a^{-1}[\max A(y) - \min A(y)]$ against (a) horizontal variance of $u^{\rm cur}(z = -0.5)$ of initial Langmuir circulation field, (b) turbulent Langmuir number La, and (c) the set of Fr and ak. Domain size is denoted with colors in (a) and (b) and with symbol shapes in (c). Domain sizes denoted with standard, S, NS, and LNS are $(L_x/\lambda, L_y/\lambda, H/\lambda) = (1, 8, 1), (1, 8, 0.5), (1, 4, 0.5)$, and $(2, 4, 0.5)$, respectively.

Figure 6 shows the y–$\tilde{z}$ plot of the horizontally low-pass-filtered downwind velocity $u^{\rm cur}$ and x-component vorticity $\hat{\zeta}^x$ from WRS and CL runs of F30. The low-pass filter is taken by first taking x average and then spectrally filtering out y variations with a wavelength shorter than λ. Comparing WRS and CL runs, we can find that the CL underestimates the intensity of $\hat{\zeta}^x$ near the upper surface $(-0.2\lambda \lesssim \tilde{z})$. The difference in x-component vorticity near the surface implies a difference in y-component velocity $v^{\rm cur}$ associated with the convergent/divergent flow at the surface. We consider that the weaker downwind jet in the CL run (Fig. 6; $2.5\lambda \lesssim y \lesssim 4\lambda$) results from the weaker large-scale vorticity pattern ($\hat{\zeta}^x < 0$ over $0 \lesssim y \lesssim 3\lambda$, $\hat{\zeta}^x > 0$ over $3\lambda \lesssim y \lesssim 6\lambda$) because the downwind momentum near the surface becomes less concentrated.

Figure 7 shows the y-direction power spectrum of x-averaged $\hat{\zeta}^x$ of all "standard" and F30-S cases. The spectra are smoothed and vertically averaged over two different depths, $-0.2\lambda \le \tilde{z} \le 0$ and $-0.05\lambda \le \tilde{z} \le 0$. It can be seen that, in the cases where strong wave modulation is observed (e.g., F30), the CL run underestimates

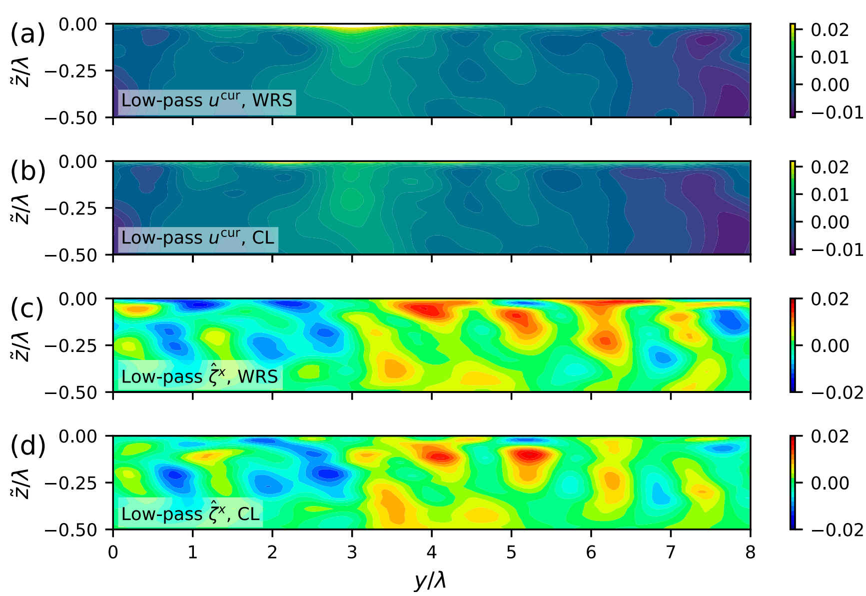

FIG. 6. Horizontally low-pass-filtered (top) downwind current velocity $u^{\rm cur}$ and (bottom) x-component vorticity $\hat{\zeta}^x$, averaged over $115T \le t \le 120T$, for (a),(c) the result of WRS of F30 and (b),(d) the result of the corresponding CL run. Only the upper half of the domain $-0.5\lambda \le \tilde{z} \le 0$ is shown.

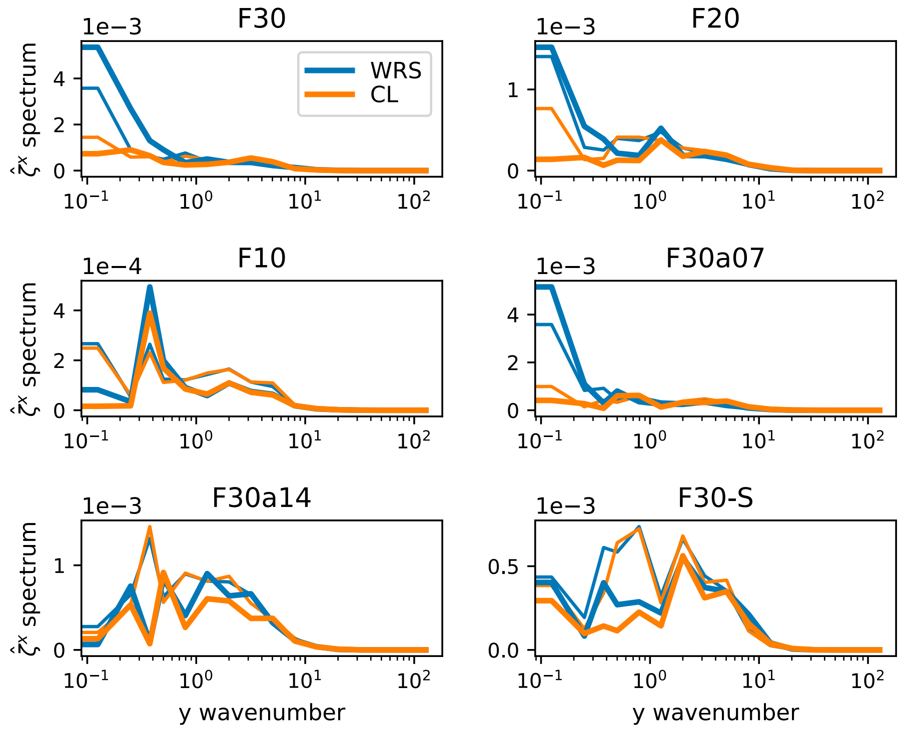

FIG. 7. The y-direction power spectrum of streamwise vorticity $\hat{\zeta}^x$ averaged in x and over $115T \le t \le 120T$. After taking power spectra at each depth, they are vertically averaged over $-0.2\lambda \le \tilde{z} \le 0$ (thin lines) or $-0.05\lambda \le \tilde{z} \le 0$ (thick lines). Blue and orange lines show the results of WRS and CL runs, respectively, for each parameter.

the low wavenumber variation of $\hat{\zeta}^x$, especially close to the surface. The difference between WRS and CL runs is larger in the cases with stronger wave modulation such as F30 and F30a07.

Such differences in jet and circulation intensity can also be found in current velocity variance. In Fig. 8, the horizontal variances of current velocity of F30 are plotted against $\tilde{z}$ for each component. The advective flux of x-component momentum $-\langle u^{\mathrm{cur}\prime} w^{\mathrm{cur}\prime}\rangle$, where angle brackets denote horizontal average and primes denote deviation from it, is also shown. The results at sections $65T \le t \le 70T$ and $115T \le t \le 120T$ are shown. Figure 8 shows that the CL run underestimates the crosswind velocity v^{cur} variance near the surface ($-0.1\lambda \lesssim \tilde{z}$), as expected from the vorticity pattern. At the surface, the difference of v^{cur} variance between WRS and CL reaches about 30% in this case. Consistently with the difference in the crosswind velocity, the vertical velocity w^{cur} variance is also underestimated in the CL run. The difference is not so large as v^{cur}, presumably because the shapes of underestimated vortices are thin in vertical (Fig. 6). The variance of the downwind velocity u^{cur} is also underestimated in the CL run, and the difference seems to become stronger and deeper as the simulation proceeds. No significant differences are seen in the momentum flux $-\langle u^{\mathrm{cur}\prime} w^{\mathrm{cur}\prime}\rangle$.

d. Vorticity budget analysis

To investigate the cause of the differences found in the circulation intensity between WRS and CL, we examine the streamwise (x component) vorticity budget of

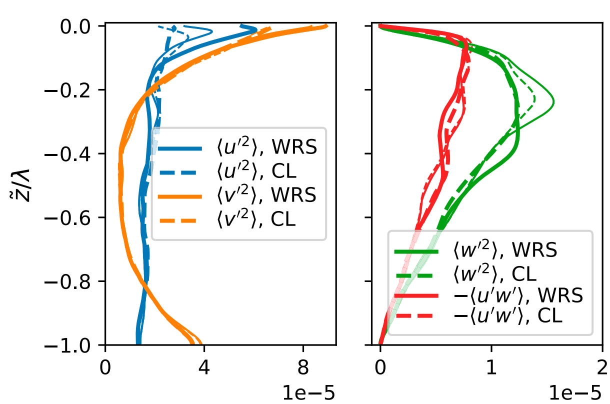

FIG. 8. Vertical profile of horizontal (co)variance of current velocity ($u^{\mathrm{cuf}}, v^{\mathrm{cur}}, w^{\mathrm{cur}}$) of WRS and CL runs of the F30 case. Solid and dashed lines show the results of WRS and CL runs, respectively. Thin and thick lines show the results wave averaged over $65T \le t \le 70T$ and $115T \le t \le 120T$, respectively. In the legend, superscript "cur" is omitted, the angle brackets denote horizontal average, and the primes denote the mean deviation from it.

the F30 case. In the VL coordinate, the x-component vorticity equation is written as follows:

$$\partial_{\tilde{t}}(h\zeta^x) = \underbrace{-\tilde{\nabla}\cdot(h\mathbf{u}\zeta^x) - \partial_{\tilde{z}}(h\omega\zeta^x)}_{\text{advection}} + \underbrace{\zeta^{\mathbf{x}}\cdot[h\tilde{\nabla}u - (\tilde{\nabla}z)\partial_{\tilde{z}}u] + \zeta^z\partial_{\tilde{z}}u}_{\text{stretching/tilting}} + (\text{visc}). \tag{16}$$

The first two terms on the rhs are vorticity advection, and the next three terms are vorticity stretching and tilting induced by velocity gradient. The last term on the rhs represents the viscous diffusion effect, and its detailed form is not explicitly shown. After temporal wave-averaging, we further decompose this equation into the following form to separate the influences of the Stokes drift (denoted with superscript St), currents (denoted with cur), and fluctuations whose time scale shorter than wave average interval (denoted with fast).

$$\partial_{\tilde{t}}(\overline{h\zeta^x}) = \mathscr{A}^{\mathrm{St}} + \mathscr{A}^{\mathrm{cur}} + \mathscr{A}^{\mathrm{fast}} + \mathscr{T}^{\mathrm{St}} + \mathscr{T}^{\mathrm{cur}} + \mathscr{T}^{\mathrm{fast}} + (\text{visc}). \tag{17}$$

Here, $\mathscr{A}$ and $\mathscr{T}$ denote advection and tilting/stretching, respectively, and each term is evaluated as follows:

$$\mathscr{A}^{\mathrm{St}} = -\tilde{\nabla}\cdot(\overline{h}\mathbf{u}^{\mathrm{St}}\hat{\zeta}^x) - \partial_{\tilde{z}}(\overline{h}\omega^{\mathrm{St}}\hat{\zeta}^x), \tag{18a}$$

$$\mathscr{A}^{\mathrm{cur}} = -\tilde{\nabla}\cdot(\overline{h}\mathbf{u}^{\mathrm{cur}}\hat{\zeta}^x) - \partial_{\tilde{z}}(\overline{h}\omega^{\mathrm{cur}}\hat{\zeta}^x), \tag{18b}$$

$$\mathscr{A}^{\mathrm{fast}} = -\tilde{\nabla}\cdot(\overline{h\mathbf{u}\zeta^x}) - \partial_{\tilde{z}}(\overline{h\omega\zeta^x}) - (\mathscr{A}^{\mathrm{St}} + \mathscr{A}^{\mathrm{cur}}), \tag{18c}$$

$$\mathscr{T}^{\mathrm{St}} = \hat{\zeta}^{\mathbf{x}}\cdot[\overline{h}\tilde{\nabla}u^{\mathrm{St}} - (\tilde{\nabla}\overline{z})\partial_{\tilde{z}}u^{\mathrm{St}}] + \hat{\zeta}^z\partial_{\tilde{z}}u^{\mathrm{St}}, \tag{18d}$$

$$\mathscr{T}^{\mathrm{cur}} = \hat{\zeta}^{\mathbf{x}}\cdot[\overline{h}\tilde{\nabla}u^{\mathrm{cur}} - (\tilde{\nabla}\overline{z})\partial_{\tilde{z}}u^{\mathrm{cur}}] + \hat{\zeta}^z\partial_{\tilde{z}}u^{\mathrm{cur}}, \quad \text{and} \tag{18e}$$

$$\mathscr{T}^{\mathrm{fast}} = \overline{\zeta^{\mathbf{x}}\cdot[h\tilde{\nabla}u - (\tilde{\nabla}z)\partial_{\tilde{z}}u]} + \overline{\zeta^z\partial_{\tilde{z}}u} - (\mathscr{T}^{\mathrm{St}} + \mathscr{T}^{\mathrm{cur}}). \tag{18f}$$

Contributions from Stokes drift and current together form the contribution from the Lagrangian mean flow. The CL equation essentially approximates this equation with $\mathscr{A}^{\mathrm{fast}} + \mathscr{T}^{\mathrm{fast}} = 0$. In our CL run, prescribed Stokes drift only contains downwind component and is horizontally uniform, so $\mathscr{A}^{\mathrm{St}} = -\partial_{\tilde{x}}(\overline{h}u^{\mathrm{St}}\hat{\zeta}^x)$ and $\mathscr{T}^{\mathrm{St}} = \hat{\zeta}^z\partial_{\tilde{z}}u^{\mathrm{St}}$.

We first investigate the relative importance of these terms in driving LCs. Figure 9 shows a y–$\tilde{z}$ plot of vorticity $\hat{\zeta}^x$, vorticity tendency $\partial_{\tilde{t}}(\overline{h\zeta^x})$, Lagrangian mean effect $\mathscr{A}^{\mathrm{St}} + \mathscr{T}^{\mathrm{St}} + \mathscr{A}^{\mathrm{cur}} + \mathscr{T}^{\mathrm{cur}}$, fast motion effect $\mathscr{A}^{\mathrm{fast}} + \mathscr{T}^{\mathrm{fast}}$, and viscosity term (evaluated as the residual). The plotted variables are averaged in x. The patterns of vorticity (Fig. 9a) and the terms of Eq. (17) (Figs. 9b–e) are both dominated by small-scale eddies. It can be found that the temporal evolution of vorticity is mostly attributed to the Lagrangian mean effects, which means that the CL formulation is a good approximation in this case, as long as spatially varying u^{St} field is correctly prescribed.

To have a closer look at the contribution of each term to the growth/decay of circulations at different scales, we conduct a spectral analysis. The temporal evolution of the power spectrum of $\hat{\zeta}^x$ (Fig. 7) follows the cospectrum (real part of the cross spectrum) of $\hat{\zeta}^x$ and the rhs terms of Eq. (17). Figure 10 shows the cospectrum of $\hat{\zeta}^x$ and each term in WRS and CL runs of F30. The "fast" terms are insignificant and are not plotted. The cospectrum is evaluated at $10T \le t \le 120T$ to study the integrated effect to reach the final state (Fig. 7). The whole period is divided into 22 sections with $5T$ period, the cospectra is computed at each section (averaged over $-0.2\lambda \le \tilde{z} \le 0$), and then the composite of all the temporal sections is taken.

From Fig. 10a, it can be found that the vorticity tilting due to the Stokes drift shear $\mathscr{T}^{\mathrm{St}}$ contributes to all the scales of the circulations and that the viscous diffusion and advection counteract. As expected, a major difference between WRS and CL runs can be found at small wavenumbers, where the CL run underestimated the circulation intensity.

We found that the cospectrum of $\hat{\zeta}^x$ and $\mathscr{T}^{\mathrm{St}}$, denoted as $\mathrm{Cosp}(\hat{\zeta}^x, \mathscr{T}^{\mathrm{St}})$, mainly consisted of the following two terms:

$$\mathrm{Cosp}(\hat{\zeta}^x, \mathscr{T}^{\mathrm{St}}) \approx \mathrm{Cosp}(\hat{\zeta}^x, \mathscr{T}_h^{\mathrm{St}}) + \mathrm{Cosp}(\hat{\zeta}^x, \mathscr{T}_v^{\mathrm{St}}), \tag{19}$$

where $\mathscr{T}_h^{\mathrm{St}} \equiv \overline{h}\hat{\zeta}^y\partial_{\tilde{y}}u^{\mathrm{St}}$ and $\mathscr{T}_v^{\mathrm{St}} \equiv \hat{\zeta}^z\partial_{\tilde{z}}u^{\mathrm{St}}$ represent the tilting of vorticity from the y and z directions to the x direction, respectively. In the CL run, the prescribed u^{St} only varies in z, so $\mathscr{T}^{\mathrm{St}} = \mathscr{T}_v^{\mathrm{St}}$.

The cospectra of vorticity and the decomposed tilting terms are plotted in Fig. 10b. At small scales (wavenumber between $\sim 10^0$ and $\sim 10^1$) where small-scale LCs are active, $\mathscr{T}_v^{\mathrm{St}}$ mostly explains the total contribution of Stokes tilting, and the CL run well reproduces the effect. This can be understood as the CL2 mechanism (Leibovich 1983). At large scales, however, $\mathscr{T}_h^{\mathrm{St}}$ becomes significant due to the horizontal shear of the Stokes drift induced by the wave modulation (Fig. 2). Since the prescribed Stokes drift is horizontally uniform in the CL run, the effect cannot be reproduced, leading to an underestimation of circulation intensity at large scales.

The overall mechanism of the simulated circulation intensification at large scales is illustrated in Fig. 11a. Consider a situation where wind and wave directions are aligned. When there is a preexisting jet structure

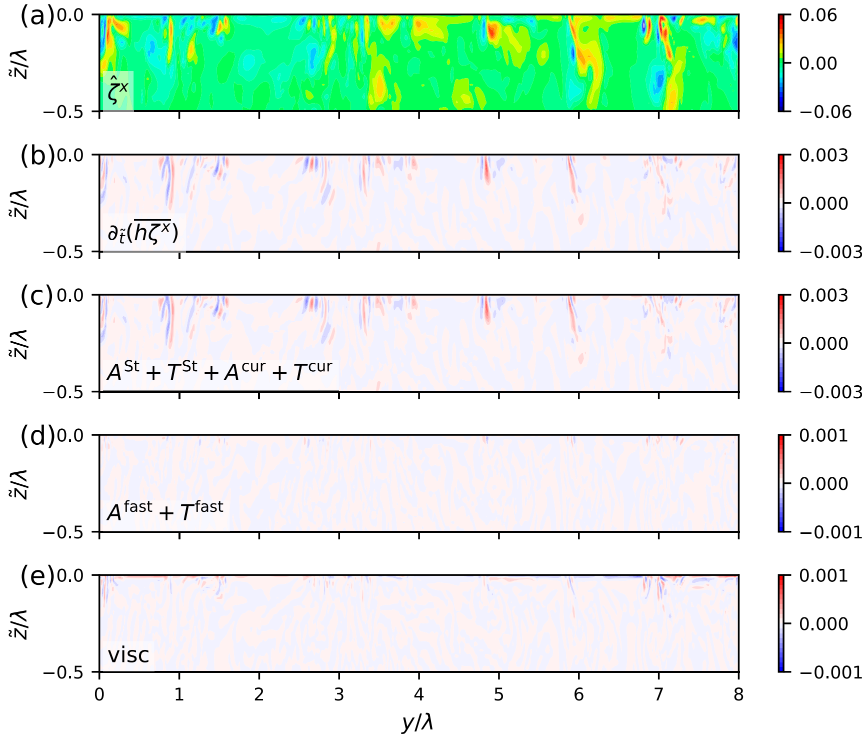

FIG. 9. The y–$\tilde{z}$ plots of (a) streamwise vorticity $\hat{\zeta}^x$, (b) its tendency $\partial_{\tilde{t}}(h\zeta^x)$, (c) Lagrangian mean terms $\mathscr{A}^{\rm St}+\mathscr{T}^{\rm St}+\mathscr{A}^{\rm cur}+\mathscr{T}^{\rm cur}$, (d) fast-motion terms $\mathscr{A}^{\rm fast}+\mathscr{T}^{\rm fast}$, and (e) viscosity term of the x-component vorticity equation [Eq. (17)]. Results are from WRS of the F30 case and are averaged in x and over $115T \le t \le 120T$. Only the upper half of the domain $-0.5\lambda \le \tilde{z} \le 0$ is shown. Note that the range of the color bar is narrower in (d) and (e).

associated with LCs [possibly driven by the classical CL2 mechanism illustrated in Fig. 11b], the jet refracts the waves, making them modulated in crosswind direction. The modulation leads to the crosswind shear of Stokes drift velocity, and the shear tilts the crosswind vorticity (associated with the wind-driven shear current) to the downwind direction. The forced downwind vorticity is the same sign as the preexisting LCs, so they are

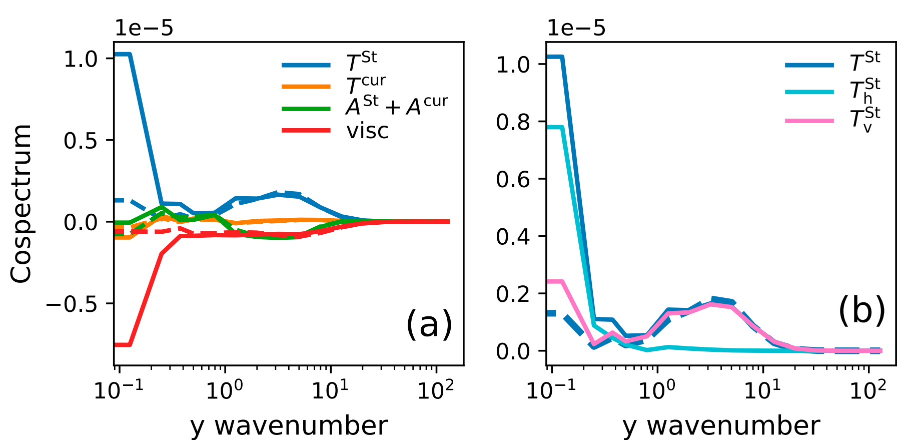

FIG. 10. (a) The y-direction cospectrum of streamwise vorticity $\hat{\zeta}^x$ and major terms in the vorticity equation [Eq. (17)] of the F30 case. Solid and dashed lines show the result of WRS and CL runs, respectively. The cospectrum is calculated by averaging in the vertical direction over $-0.2\lambda \le \tilde{z} \le 0$ at every $5T$ sections in the period $10T \le \tilde{z} \le 120T$, and then by taking composite over the period. (b) The cospectrum of $\mathscr{T}^{\rm St}$ and its decomposed terms [Eq. (19)].

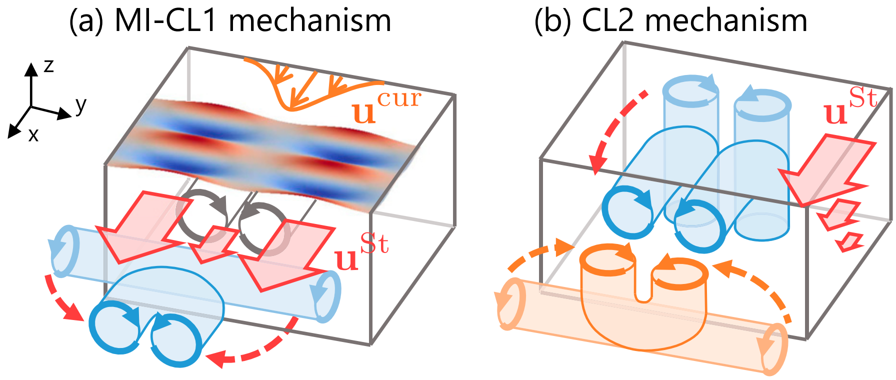

FIG. 11. Sketch of the driving mechanisms of LCs. Tubes represent vorticity, and red arrows represent the Stokes drift profile. (a) The sketch of the modulation-induced CL1 mechanism, where the modulated surface waves are shown with the three-dimensional surface plot. (b) The sketch of the CL2 instability mechanism (Leibovich 1983), where the orange tube is vorticity associated with wind-driven shear current, which is bent by the streamwise circulation to intensify preexisting vertical vorticity.

intensified. Since the wave modulation tends to occur at horizontal scales larger than a wavelength, the mechanism only affects the circulation with such scales.

The mechanism proposed here involves the tilting of crosswind vorticity by horizontally sheared Stokes drift as in the CL1 mechanism first proposed by Craik and Leibovich (1976). For this reason, we call it "modulation-induced CL1" or "MI-CL1" mechanism. In the original CL1 mechanism, it is assumed that interference of two crossing waves produces the horizontal sheared Stokes drift. Therefore, the CL1 mechanism requires the relative phase between the two waves to be locked for hundreds of wave periods (Leibovich 1983), which makes the mechanism less plausible to be the major driving mechanism of LCs. On the other hand, in the MI-CL1 mechanism, the preexisting LCs modulate waves and induce horizontally sheared Stokes drift in a favorable way to themselves, and the wave field does not need to hold certain phase relations.

5. Discussion and conclusions

Through a vorticity budget analysis of WRS in an idealized condition, a new mechanism of intensifying LCs that involves a mutual interaction of waves and currents is found. When there are preexisting LCs [possibly produced by the CL2 mechanism (Leibovich 1983)], the accompanying downwind jet current refracts the wave, causing amplitude to vary in crosswind direction. The resulting horizontal variation of Stokes drift tilts the vorticity of wind-driven shear current to downwind direction, intensifying the preexisting LCs. It is suggested that the structure and intensity of the preexisting LCs control the magnitude of modulation. LCs produced under a large turbulent Langmuir number $\mathrm{La} = \mathrm{Fr}^{1/2}(ak)^{-1}$ (i.e., large Fr and small ak) are likely to cause stronger modulation. This condition corresponds to a young sea. Also, the modulation is affected by the extent of Langmuir cells, and larger cells are likely to cause stronger modulation. The domain depth-dependence of the wave modulation suggests that the mixed layer depth may affect the intensity of modulation through the size of LCs.

To reproduce this intensification mechanism using the CL equation, the current-dependent Stokes drift field needs to be prescribed. However, in this case, the use of the wave action conservation law (e.g., McWilliams et al. 2004; Smith 2006; Uchiyama et al. 2010) to prescribe the Stokes drift is not justified because the scales of currents and waves are not separated. WRS will be a useful approach to examine possible models of wave fields affected by small-scale currents (e.g., Smith 1983; Suzuki 2019).

The impact of wave modulation on current is expected to be especially important close to the surface for the following reasons. First, in our results, a large difference with and without wave modulation is found near the surface (Figs. 6 and 8), where the crosswind vorticity (to be tilted downwind) is strong. Second, when waves with a broad spectrum are present, shorter waves will be most strongly affected by the current field, and shorter waves have a strong influence on the Stokes drift close to the surface. The intensity of LCs close to the surface is an important factor in the air–sea exchange of heat and gas.

Let us roughly estimate the scale of waves affected by the currents using a result of the CL equation for reference. McWilliams et al. (2012) reports the LES result of a wave-affected Ekman layer problem, where the

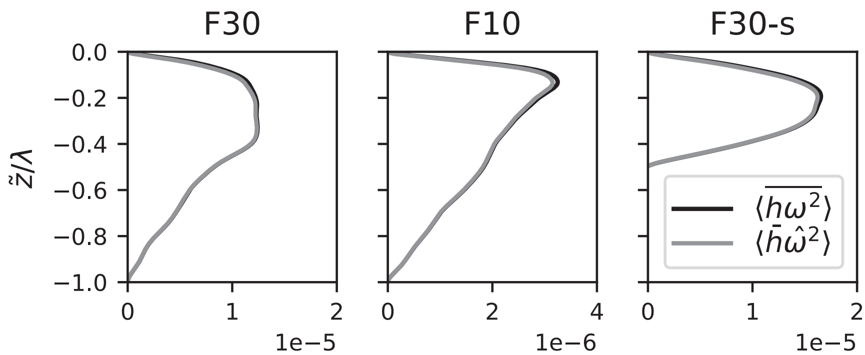

FIG. A1. Vertical profiles of the thickness-weighted variances of the cross-coordinate velocity ω in the WRS runs of the F30, F10, and F30-s cases. Total variance $\langle \overline{h\omega^2} \rangle$ (the overbar denotes temporal average, and angle brackets denote the horizontal average) is shown with black lines. Variance of temporal-averaged variance $\langle \overline{h\omega^2} \rangle$ is shown with gray lines. Temporal average is evaluated at $115T \leq t \leq 120T$ of each case.

Stokes drift profile is calculated from a broad-banded wave spectrum with a peak wavelength of 84 m. In their result, the value of σ_u^2/u_*^2 (where σ_u denotes horizontal standard deviation of u) reaches about 2 above 40-m depth (their Fig. 4). Using $u_* = 0.019\,\mathrm{m\,s^{-1}}$ and approximating σ_u/u_* with a fixed value 1.4, we can estimate that $\sigma_u/c \approx 0.0023$ and 0.0046 for waves with $\lambda = 84$ and 21 m, respectively. In the present study, F10 case shows a certain amount of wave modulation with $\sigma_u/c = 0.0043$ (Fig. 5). Therefore, we expect that the waves with $\lambda = 21$ m in their settings would be influenced by the currents as much as our F10 case, and that the influence will become more significant for shorter waves. Of course, the mutual interaction of waves and currents changes the turbulence statistics, so the above estimates may be modified. Since the mutual interaction intensifies the LCs, the modification would make the current effect on waves occur more easily.

Because of many simplifications of our simulation designs and the limited integration period, the discussion above remains somewhat qualitative, and further effort to quantify the wave–current mutual interaction must be made. First, as discussed in section 4b, the strength of wave modulation observed in our WRS is strongly affected by the extent of the computational domain. With a larger domain in crosswind and vertical directions, modulation becomes stronger, and with a larger domain in downwind direction, modulation becomes weaker. The reality corresponds to the situation where the horizontal domain extent approaches infinity. Therefore, we cannot conclude if the net effect of horizontal boundaries is magnifying or reducing the wave modulation without further experiments. Second, the effect of system rotation is not considered in our simulations. It is known from the LES of the CL equation that the Coriolis effect tends to rotate the axes of LCs to the right in the Northern Hemisphere (e.g., McWilliams et al. 1997). Because the wave propagation direction is less aligned with the jets, the current effect on waves observed in this study could be somewhat reduced. Third, we employed uniform viscosity rather than spatially variable eddy viscosity because we consider that the effects of turbulence on wave motions cannot be represented through the conventional eddy viscosity form, as pointed out by Ardhuin and Jenkins (2006). The turbulence effects may alter the magnitude of wave modulation through the structure of Langmuir cells (e.g., the width of the jet). However, we may expect that our results are insensitive to the form of viscosity because the simulated flow field is fairly turbulent and it is the large-scale circulations that strongly affected the waves. To examine the above discussion, further study is needed to incorporate the effects of turbulence in the framework of WRS.

The horizontal variation of wave amplitude will likely lead to nonuniform wave breaking. In our case, waves are more likely to break at locations off the downwind jet, where wave amplitude is large. Such nonuniformity of breaking will further modify the wave–current interaction processes illustrated here (Fig. 11) because localized wave breaking will impose vertical vorticity (e.g., Pizzo and Melville 2013). Since the sign of imposed vertical vorticity is opposite to the preexisting one (in other words, downwind momentum is imposed off the downwind jet), the coupling with wave breaking may lead to a formation of a negative feedback process. If such processes need to be properly simulated without explicit treatment of breaking, representations of momentum input into the mixed layer must be reconsidered.

Acknowledgments. This research is supported by MEXT KAKENHI JP15H05824 and JSPS KAKENHI JP17J07923 and JP19H01968.

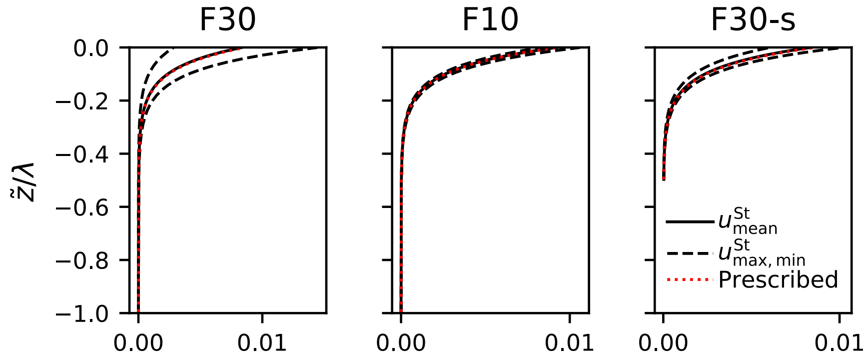

FIG. A2. Vertical profiles of the Stokes drift u^{St} evaluated in the WRS runs of the (left) F30, (center) F10, and (right) F30-s cases, and the corresponding prescribed profiles [Eq. (11)]. WRS results (shown with black lines) are evaluated at $115T \le t \le 120T$ and averaged in x. Prescribed profiles (shown with red dots, almost overlapped with black solid lines) are evaluated at $t = 117.5T$. Solid lines show the y-averaged profile, and dashed lines show maximum and minimum (in y) profiles.

APPENDIX

Performance of VL Analysis

In this study, the mathematical framework of the VL coordinate system (Mellor 2003; Aiki and Greatbatch 2012) is imitated by using the linear solution of irrotational surface waves (section 3). In this section, it is shown that the above method approximates the theoretical framework well.

In the VL system, the vertical coordinate surfaces ($\tilde{z}$ surfaces) follow the high-frequency (wave) motions as material surfaces. Therefore, the cross-surface velocity ω should only contain low-frequency temporal variations. In Fig. A1, the vertical profiles of the thickness-weighted variances of ω are shown. Denoting horizontal average with angle brackets, the total variance is $\langle \overline{h\omega^2} \rangle$. Using the definition of thickness-weighted average, defining the deviation from the average as $(\cdot)'' \equiv (\cdot) - \widehat{(\cdot)}$, the total variance can be decomposed as $\overline{h\omega^2} = \overline{h}\hat{\omega}^2 + \overline{h\omega''^2}$ (cf. Aiki and Greatbatch 2012). The horizontal average $\langle \overline{h}\hat{\omega}^2 \rangle$ represents the contribution of the low-frequency motion to the total variance. Fig. A1 shows that $\langle \overline{h\omega^2} \rangle \approx \langle \overline{h}\hat{\omega}^2 \rangle$ (where temporal average is evaluated over $115T \le t \le 120T$), which means that the high-frequency variation of ω is small. Therefore, $\tilde{z}$ surfaces follow the wave motions well.

The Stokes drift was evaluated as the thickness-weighted average of wave orbital velocity. It is known that the thickness-weighted wave orbital velocity in the VL coordinate agrees with the classical Stokes drift profile (Stokes 1847) using the linear solution of monochromatic surface waves (Mellor 2003). Here we show that the profile evaluated in the WRS result does agree with the classical profile to the leading order. Fig. A2 shows the vertical profiles of the x-component Stokes drift u^{St} evaluated in the simulations and the prescribed ones using the linear theory [Eq. (11)]. In each case, wave average is taken over $115T \le t \le 120T$, after which the field is averaged in x, leaving y and $\tilde{z}$ dependence of u^{St}. Maximum in y, minimum in y, and y-averaged profiles are shown for each case. It can be seen that the horizontally averaged Stokes drift profile agrees well with the linear solution, even in F30 where the wave modulation is strongest. This result also suggests that the estimation of viscous wave decay based on the linear theory (the decay coefficient of $e^{-4\nu k^2 t}$) is appropriate, at least for the horizontally averaged profiles.

REFERENCES

Aiki, H., and R. J. Greatbatch, 2012: Thickness-weighted mean theory for the effect of surface gravity waves on mean flows in the upper ocean. *J. Phys. Oceanogr.*, **42**, 725–747, https://doi.org/10.1175/JPO-D-11-095.1.

Andrews, D. G., and M. E. McIntyre, 1978: An exact theory of nonlinear waves on a Lagrangian-mean flow. *J. Fluid Mech.*, **89**, 609–646, https://doi.org/10.1017/S0022112078002773.

Ardhuin, F., and A. D. Jenkins, 2006: On the interaction of surface waves and upper ocean turbulence. *J. Phys. Oceanogr.*, **36**, 551–557, https://doi.org/10.1175/JPO2862.1.

Belcher, S. E., and Coauthors, 2012: A global perspective on Langmuir turbulence in the ocean surface boundary layer. *Geophys. Res. Lett.*, **39**, L18605, https://doi.org/10.1029/2012GL052932.

Craik, A. D. D., 1977: The generation of Langmuir circulations by an instability mechanism. *J. Fluid Mech.*, **81**, 209–223, https://doi.org/10.1017/S0022112077001980.

——, and S. Leibovich, 1976: A rational model for Langmuir circulations. *J. Fluid Mech.*, **73**, 401–426, https://doi.org/10.1017/S0022112076001420.

D'Asaro, E. A., 2014: Turbulence in the upper-ocean mixed layer. *Annu. Rev. Mar. Sci.*, **6**, 101–115, https://doi.org/10.1146/annurev-marine-010213-135138.

Fujiwara, Y., Y. Yoshikawa, and Y. Matsumura, 2018: A wave-resolving simulation of Langmuir circulations with a nonhydrostatic free-surface model: Comparison with Craik–Leibovich theory and an alternative Eulerian view of the driving mechanism. *J. Phys. Oceanogr.*, **48**, 1691–1708, https://doi.org/10.1175/JPO-D-17-0199.1.

——, ——, and ——, 2019: Reply to "Comments on 'Awave-resolving simulation of Langmuir circulations with a nonhydrostatic free-surface model: Comparison with Craik–Leibovich theory and an alternative Eulerian view of the driving mechanism.'" *J. Phys. Oceanogr.*, **49**, 889–892, https://doi.org/10.1175/JPOD-19-0015.1.

Guo, X., and L. Shen, 2009: On the generation and maintenance of waves and turbulence in simulations of free-surface turbulence. *J. Comput. Phys.*, **228**, 7313–7332, https://doi.org/10.1016/j.jcp.2009.06.030.

——, and ——, 2013: Numerical study of the effect of surface waves on turbulence underneath. Part I. Mean flow and turbulence vorticity. *J. Fluid Mech.*, **733**, 558–587, https://doi.org/10.1017/jfm.2013.451.

——, and ——, 2014: Numerical study of the effect of surface wave on turbulence underneath. Part 2. Eulerian and Lagrangian properties of turbulence kinetic energy. *J. Fluid Mech.*, **744**, 250–272, https://doi.org/10.1017/jfm.2014.43.

Holthuijsen, L. H., 2010: *Waves in Oceanic and Coastal Waters*. Cambridge University Press, 404 pp.

Kawamura, T., 2000: Numerical investigation of turbulence near a sheared air–water interface. Part 2: Interaction of turbulent shear flow with surface waves. *J. Mar. Sci. Technol.*, **5**, 161–175, https://doi.org/10.1007/s007730070002.

Kenyon, K. E., 1969: Stokes drift for random gravity waves. *J. Geophys. Res.*, **74**, 6991–6994, https://doi.org/10.1029/JC074i028p06991.

Lamb, H., 1932: *Hydrodynamics*. 6th ed. Cambridge University Press, 738 pp.

Langmuir, I., 1938: Surface motion of water induced by wind. *Science*, **87**, 119–123, https://doi.org/10.1126/science.87.2250.119.

Leibovich, S., 1977: Convective instability of stably stratified water in the ocean. *J. Fluid Mech.*, **82**, 561–581, https://doi.org/10.1017/S0022112077000846.

——, 1980: On wave-current interaction theories of Langmuir circulations. *J. Fluid Mech.*, **99**, 715–724, https://doi.org/10.1017/S0022112080000857.

——, 1983: The form and dynamics of Langmuir circulations. *Annu. Rev. Fluid Mech.*, **15**, 391–427, https://doi.org/10.1146/annurev.fl.15.010183.002135.

Li, M., and C. Garrett, 1993: Cell merging and the jet/downwelling ratio in Langmuir circulation. *J. Mar. Res.*, **51**, 737–769, https://doi.org/10.1357/0022240933223945.

——, ——, and E. Skyllingstad, 2005: A regime diagram for classifying turbulent large eddies in the upper ocean. *Deep-Sea Res. I*, **52**, 259–278, https://doi.org/10.1016/j.dsr.2004.09.004.

Longuet-Higgins, M. S., 1953: Mass transport in water waves. *Philos. Trans. Roy. Soc. London*, **A245**, 535–581, https://doi.org/10.1098/rsta.1953.0006.

McWilliams, J. C., P. P. Sullivan, and C.-H. Moeng, 1997: Langmuir turbulence in the ocean. *J. Fluid Mech.*, **334**, 1–30, https://doi.org/10.1017/S0022112096004375.

——, J. M. Restrepo, and E. M. Lane, 2004: An asymptotic theory for the interaction of waves and currents in coastal waters. *J. Fluid Mech.*, **511**, 135–178, https://doi.org/10.1017/S0022112004009358.

——, E. Huckle, J.-H. Liang, and P. P. Sullivan, 2012: The wavy Ekman layer: Langmuir circulations, breaking waves, and Reynolds stress. *J. Phys. Oceanogr.*, **42**, 1793–1816, https://doi.org/10.1175/JPO-D-12-07.1.

Mellor, G. L., 2003: The three-dimensional current and surface wave equations. *J. Phys. Oceanogr.*, **33**, 1978–1989, https://doi.org/10.1175/1520-0485(2003)033<1978:TTCASW>2.0.CO;2.

Phillips, O., 1966: *The Dynamics of the Upper Ocean*. Cambridge University Press, 336 pp.

Phillips, W. R., 2005: On the spacing of Langmuir circulation in strong shear. *J. Fluid Mech.*, **525**, 215–236, https://doi.org/10.1017/S0022112004002654.

Pizzo, N., and W. K. Melville, 2013: Vortex generation by deep-water breaking waves. *J. Fluid Mech.*, **734**, 198–218, https://doi.org/10.1017/jfm.2013.453.

Skyllingstad, E. D., and D. W. Denbo, 1995: An ocean large-eddy simulation of Langmuir circulations and convection in the surface mixed layer. *J. Geophys. Res.*, **100**, 8501–8522, https://doi.org/10.1029/94JC03202.

Smith, J. A., 1983: On surface gravity waves crossing weak current jets. *J. Fluid Mech.*, **134**, 277–299, https://doi.org/10.1017/S0022112083003365.

——, 2006: Wave–current interactions in finite depth. *J. Phys. Oceanogr.*, **36**, 1403–1419, https://doi.org/10.1175/JPO2911.1.

Stewart, R. H., and J. W. Joy, 1974: HF radio measurements of surface currents. *Deep-Sea Res. Oceanogr. Abstr.*, **21**, 1039–1049, https://doi.org/10.1016/0011-7471(74)90066-7.

Stokes, G. G., 1847: On the theory of oscillatory waves. *Trans. Cambridge Philos. Soc.*, **8**, 441–473.

Suzuki, N., 2019: On the physical mechanisms of the two-way coupling between a surface wave field and a circulation consisting of a roll and streak. *J. Fluid Mech.*, **881**, 906–950, https://doi.org/10.1017/jfm.2019.752.

Tsai, W., S. Chen, G. Lu, and C. S. Garbe, 2013: Characteristics of interfacial signatures on a wind-driven gravity-capillary wave. *J. Geophys. Res. Oceans*, **118**, 1715–1735, https://doi.org/10.1002/jgrc.20145.

——, ——, and ——, 2015: Numerical evidence of turbulence generated by nonbreaking surface waves. *J. Phys. Oceanogr.*, **45**, 174–180, https://doi.org/10.1175/JPO-D-14-0121.1.

——, G. Lu, J. Chen, A. Dai, and W. R. Phillips, 2017: On the formation of coherent vortices beneath nonbreaking free-propagating surface waves. *J. Phys. Oceanogr.*, **47**, 533–543, https://doi.org/10.1175/JPO-D-16-0242.1.

Uchiyama, Y., J. C. McWilliams, and A. F. Shchepetkin, 2010: Wave–current interaction in an oceanic circulation model with a vortex-force formalism: Application to the surf zone. *Ocean Modell.*, **34**, 16–35, https://doi.org/10.1016/j.ocemod.2010.04.002.

Veron, F., and W. K. Melville, 2001: Experiments on the stability and transition of wind-driven water surfaces. *J. Fluid Mech.*, **446**, 25–65, https://doi.org/10.1017/S0022112001005638.

Wang, P., and T. Özgökmen, 2018: Langmuir circulation with explicit surface waves from moving-mesh modeling. *Geophys. Res. Lett.*, **45**, 216–226, https://doi.org/10.1002/2017GL076009.

Xuan, A., B.-Q. Deng, and L. Shen, 2019: Study of wave effect on vorticity in Langmuir turbulence using wave-phase-resolved large-eddy simulation. *J. Fluid Mech.*, **875**, 173–224, https://doi.org/10.1017/jfm.2019.481.